

**OPEN ACCESS**

## Algorithm-independent optimal input fluxes for boundary identification in thermal imaging

To cite this article: K Bryan and L Caudill 2008 *J. Phys.: Conf. Ser.* **124** 012010

View the [article online](#) for updates and enhancements.

### You may also like

- [Electron microscopy for Engineers](#)  
I P Jones
- [Metallic nanofilms optical response description based on self-consistent theory](#)  
A V Andreev and S S Postnov
- [Nanophotonics for information systems](#)  
Y Fainman, K Ikeda, M Abashin et al.



**ECS**  
The  
Electrochemical  
Society  
Advancing solid state &  
electrochemical science & technology

**DISCOVER**  
how sustainability  
intersects with  
electrochemistry & solid  
state science research

# Algorithm-independent optimal input fluxes for boundary identification in thermal imaging

Kurt Bryan<sup>1</sup> and Lester Caudill<sup>2</sup>

<sup>1</sup> Department of Mathematics, Rose-Hulman Institute of Technology, Terre Haute, IN 47803, USA

<sup>2</sup> Department of Mathematics and Computer Science, University of Richmond, Richmond, VA 23173, USA

E-mail: kurt.bryan@rose-hulman.edu, lcaudill@richmond.edu

**Abstract.** An inverse boundary determination problem for a parabolic model, arising in thermal imaging, is considered. The focus is on intelligently choosing an effective input heat flux, so as to maximize the practical effectiveness of an inversion algorithm. Three different methods, based on different interpretations of the term “effective”, are presented and analyzed, then demonstrated through numerical examples. It is noteworthy that each of these flux-selection methods is independent of the particular inversion algorithm to be used.

## 1. Introduction

This paper addresses the following parabolic inverse boundary identification problem: Let  $\Omega$  be a bounded and connected region in  $\mathbb{R}^n$ , with boundary  $\partial\Omega$  consisting of two surfaces  $\Gamma$  and  $S_0$ . Let  $u = u(t, x)$  (the temperature of  $\Omega$ ) satisfy the initial-boundary value problem

$$\frac{\partial u}{\partial t} - \Delta_x u = 0, \quad x \in \Omega, \quad 0 < t < T; \quad (1)$$

$$\frac{\partial u}{\partial \eta} = g(t, x), \quad x \in \Gamma, \quad 0 < t < T; \quad (2)$$

$$\frac{\partial u}{\partial \eta} = 0, \quad x \in S_0, \quad 0 < t < T; \quad (3)$$

$$u(0, x) = 0, \quad x \in \Omega \quad (4)$$

where  $\eta$  denotes a unit outward normal vector on  $\partial\Omega$ . The function  $g$  represents an input heat flux (at least after suitable rescaling) on  $\Gamma$ , while we assume that the surface  $S_0$  is perfectly insulating. Given suitable  $\Gamma$ ,  $S_0$ , and  $g$ , determining  $u$  on  $\Omega$  over a prescribed time interval is a well-posed problem.

We consider the inverse problem in which the surface  $\Gamma$  is accessible for temperature/flux measurements, while  $S_0$  is considered inaccessible, and is to be determined from the Cauchy data  $g(t, x)$  and

$$u(t, x) \text{ for } x \in \Gamma \text{ and } t \in (T_1, T_2). \quad (5)$$

The authors present a numerical algorithm for this inverse problem in [2], where they view the input flux  $g$  as forward data, and the resulting surface temperature (5) as the overposed data.

As we begin to consider a practical implementation of this algorithm, it becomes clear that our algorithm (like any other) has a number of design parameters which must be specified. In addition to algorithm-specific parameters (which will not be addressed here), there are some design parameters which, by the nature of this inverse problem, must be present in *any* algorithm used to numerically solve it. Two such parameters which are of particular interest to us are

- choice of the input flux  $g(t, x)$ .
- choice of the time interval over which to measure the Dirichlet data on  $\Gamma$ .

In this paper, we report preliminary results of an investigation of the first parameter choice, i.e. we consider ways to intelligently choose the input flux function  $g(t, x)$  in (2). (The second parameter choice – data time window – will be addressed in a future paper.) The issue here is that different choices for  $g$ , as will be seen later, will result in reconstructions that differ in quality and accuracy. Consequently, we seek to characterize input fluxes that may be considered “optimal” in an appropriate sense. The first task is to determine exactly what will be meant by the term “optimal”.

In this work, we present two different approaches to making precise the term “optimal input flux,” and investigate the consequences of each. The first, which is the focus of Section 2, is cast within a Hilbert space framework. This approach is modeled on the important work of Isaacson, Cheney, and co-authors (see [3, 5, 8, 9]), on the topic of optimal current patterns for the impedance tomography problem. The second approach to “optimal input fluxes” is based more upon intuitive physical considerations, and is the subject of Section 3. For each, optimality is defined in terms of a chosen flux’s ability to recognize differences between two different  $S_0$  surfaces. This perspective makes sense within the context of damage assessment, where the extent of damage to a sample is determined by the extent of its variation from a damage-free version of the same sample.

In Section 4, we present the results of numerical experiments designed to compare the performances of these different fluxes on a model problem. Section 5 addresses the consequences of finite-precision measurements within this context.

## 2. Hilbert Space Approach

As noted, we will characterize optimality of fluxes in terms of each flux’s ability to distinguish between two different choices of  $S_0$ . To this end, we consider two such surfaces which, for added confusion, we will label  $S_1$  and  $S_2$ . We consider two copies of the IBVP (1)-(4), one for  $S_1$  and one for  $S_2$ . We will denote by  $\Omega_j$  and  $u_j = u_j(t, x; g)$  the domain and IBVP solution, respectively, corresponding to (1)-(4) with a specific choice of input flux  $g$  and with  $S_0$  replaced by  $S_j$ . (See Figure 1.)

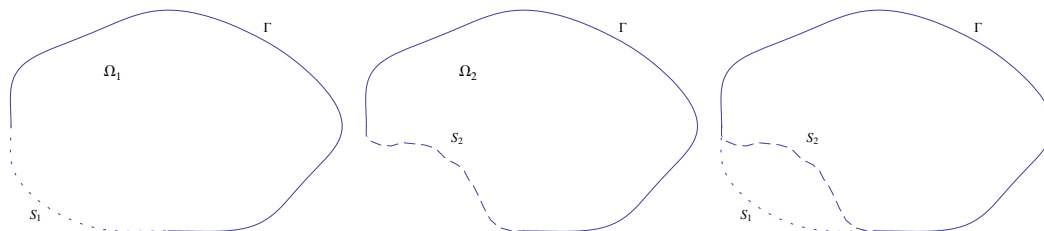


**Figure 1.** The domains  $\Omega_1$  and  $\Omega_2$  (left and center), and these two domains overlaid.

For simplicity of presentation, we will assume that  $\Omega_2 \subseteq \Omega_1$ , although this assumption can be relaxed.

### 2.1. First Definition of “Optimality”.

The following approach follows the important work of D. Isaacson and co-authors [3, 5, 8, 9] regarding distinguishability for the impedance tomography problem. Let  $G$  be a set of admissible functions  $g$  for the IBVP (1)-(4), and define an inner product for  $f, g \in G$  by

$$\langle f, g \rangle \equiv \int_0^T \int_{\Gamma} f g \, ds dt. \quad (6)$$

We denote by  $\mathcal{G}$  the set  $G$  equipped with this inner product, completing it if necessary to make  $\mathcal{G}$  a Hilbert space. Let  $B(\mathcal{G})$  represent the surface of the unit ball in  $\mathcal{G}$ . For  $j = 1, 2$ , define the partial Neumann-to-Dirichlet operator  $L_j : \mathcal{G} \rightarrow \mathcal{G}$  by

$$L_j(g) = u_j|_{\Gamma \times [0, T]}, \quad \text{for } g \in \mathcal{G}.$$

Thus,  $L_j$  maps the input flux to the measured data. We will say that an *optimal input flux* is a member  $\hat{g}$  of  $B(\mathcal{G})$  for which

$$\|u_1(\hat{g}) - u_2(\hat{g})\|^2 = \|L_1(\hat{g}) - L_2(\hat{g})\|^2 = \sup_{g \in B(\mathcal{G})} \|L_1(g) - L_2(g)\|^2, \quad (7)$$

where the norm is the one induced by the inner product (6). In words, this simply says that the optimal flux is the flux which produces the largest (in the  $L^2$ -sense) difference between the measured data on the two domains.

Following Isaacson, we define an operator  $\mathcal{L} : \mathcal{G} \rightarrow \mathcal{G}$  by

$$\mathcal{L} = (L_1^* - L_2^*)(L_1 - L_2),$$

where  $*$  represents the Hilbert space adjoint. Thus, (7) can be formulated equivalently as

$$\|L_1(\hat{g}) - L_2(\hat{g})\|^2 = \sup_{g \in B(\mathcal{G})} \langle \mathcal{L}g, g \rangle. \quad (8)$$

Noting that  $\mathcal{L}$  is compact, self-adjoint, and non-negative, the spectrum of  $\mathcal{L}$  consists of a discrete set  $\{\lambda_n\}$  of real numbers with  $\lambda_n \searrow 0$ , and a corresponding orthonormal basis  $\{\phi_n\}$  of eigenfunctions. Then, from the Minimax Principle (see [6], pp. 405-406), we conclude, under the assumption that  $\lambda_1$ , the largest eigenvalue of  $\mathcal{L}$ , is simple, that  $\hat{g}$  in (8) should be taken to be  $\pm\phi_1$ , the first normalized eigenfunction of  $\mathcal{L}$ . More precisely, we have the following result.

**Theorem 2.1** *The input flux  $g \in B(\mathcal{G})$  that maximizes (in the sense of the norm induced by the inner product (6)) the difference in the boundary data between  $S_1$  and  $S_2$  is  $\hat{g} = \phi_1$ , where  $\phi_1$  is a normalized eigenfunction corresponding to the largest eigenvalue  $\lambda_1$  of the operator  $\mathcal{L} = (L_1^* - L_2^*)(L_1 - L_2)$ . Moreover, for this choice of  $\hat{g}$ ,*

$$\|L_1(\hat{g}) - L_2(\hat{g})\| = \sqrt{\lambda_1}.$$

**Proof.** In light of the discussion leading up to the statement of the theorem, the only remaining issue is the last equality, which is an immediate consequence of the Minimax Principle [6].  $\square$

We now illustrate two optimal fluxes, obtained by numerically approximating the eigenfunction in Theorem 2.1. The approximation method is based on the following result, which is essentially the Power Method (see, e.g., [10]).

**Result 2.1** Let  $\phi \in \mathcal{G}$  for which  $\langle \phi, \phi_1 \rangle \neq 0$ , and let  $n \in \mathbb{N}$ . Then,

$$\lim_{n \rightarrow \infty} \frac{\mathcal{L}^n \phi}{\|\mathcal{L}^n \phi\|} = \pm \phi_1.$$

Furthermore, if the eigenvalue  $\lambda_1$  of  $\mathcal{L}$  is simple, then the convergence is exponential.

**Proof.** Expand  $\phi$  in terms of an orthonormal basis  $\{\phi_j\}$  of eigenfunctions of  $\mathcal{L}$ :

$$\phi = \sum_{j=1}^{\infty} \langle \phi, \phi_j \rangle \phi_j.$$

Applying  $\mathcal{L}$   $n$  times yields

$$\begin{aligned} \mathcal{L}^n \phi &= \sum_{j=1}^{\infty} \langle \phi, \phi_j \rangle \lambda_j^n \phi_j \\ &= \langle \phi, \phi_1 \rangle \lambda_1^n \phi_1 + \sum_{j=2}^{\infty} \langle \phi, \phi_j \rangle \lambda_j^n \phi_j \\ &= \lambda_1^n \left( \langle \phi, \phi_1 \rangle \phi_1 + \sum_{j=2}^{\infty} \langle \phi, \phi_j \rangle \left( \frac{\lambda_j}{\lambda_1} \right)^n \phi_j \right). \end{aligned}$$

Likewise, one may compute

$$\|\mathcal{L}^n \phi\| = \lambda_1^n |\langle \phi, \phi_1 \rangle| \sqrt{1 + \sum_{j=2}^{\infty} \frac{\langle \phi, \phi_j \rangle^2}{\langle \phi, \phi_1 \rangle^2} \left( \frac{\lambda_j}{\lambda_1} \right)^{2n}}.$$

Since  $\lambda_1 > \lambda_j$ , the terms  $\left( \frac{\lambda_j}{\lambda_1} \right)^n$  decay exponentially to zero as  $n$  increases. As a result,

$$\lim_{n \rightarrow \infty} \frac{\mathcal{L}^n \phi}{\|\mathcal{L}^n \phi\|} = \frac{\langle \phi, \phi_1 \rangle \phi_1}{|\langle \phi, \phi_1 \rangle|} = \text{sgn}(\langle \phi, \phi_1 \rangle) \phi_1.$$

□

For a given input flux  $g$ ,  $L_j(g)$  is computed, for  $j = 1$  or  $2$ , by directly solving the appropriate version of the forward problem (1)-(4). To compute  $L_j^*(h)$ , for  $j = 1, 2$  and some function  $h$  defined on  $\Gamma \times [0, T]$ , we use the fact that

$$L_j^*(h) = L_j^*(h)(t, x) = L_j(\tilde{h})(T - t, x),$$

where  $\tilde{h}(t, x) = h(T - t, x)$ . So, we compute the adjoints through suitable time-reversals of the relevant solution of the forward problem.

Two such optimal fluxes, corresponding to different domain pairs, are shown in Figure 2. In each case,  $\Omega_1$  is the rectangle  $[0, 1] \times [-0.5, 0]$ . In the first example,  $\Omega_2$  is the same rectangle, with a portion of its lower boundary replaced by a smooth hump. The choice of  $\Omega_2$  in the second example is similar, but with a second, smaller, hump included. In each illustration, the magnitude of the resulting optimal flux is plotted at several fixed times, as a function of  $x$ .

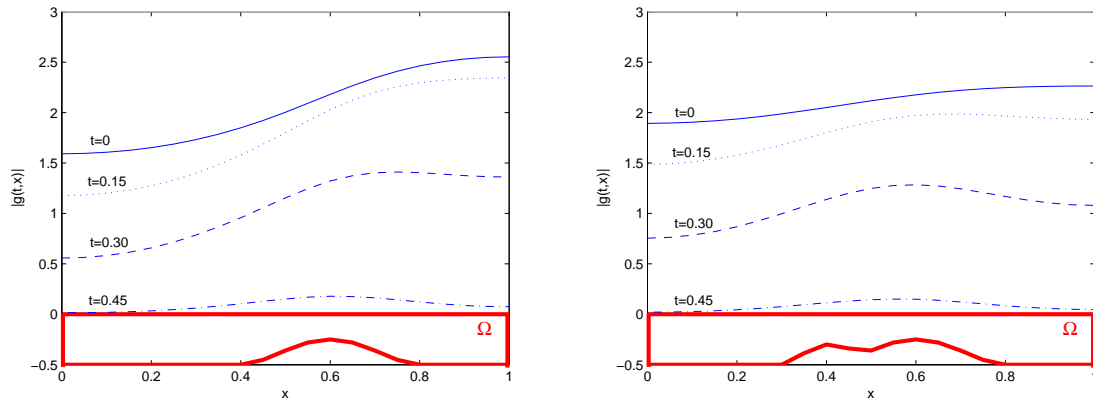


**Figure 2** Two examples of optimal fluxes.

The shapes of these flux magnitudes suggest that their effectiveness at distinguishing the two surfaces stems from their ability to induce a heat flow, of sorts, across the back surface, in such a way as to sample the surface most effectively.

### 3. The “Heat Content” Approach

Returning to the inverse problem of Section 1, we will now consider a somewhat different perspective on the optimal flux issue. We still seek the input flux that best distinguishes between two surfaces  $S_1$  and  $S_2$  – the change is in the meaning of “best distinguishes.” Specifically, denote by  $D$  the region bounded by the surfaces  $S_1$  and  $S_2$ . (See Figure 3.)

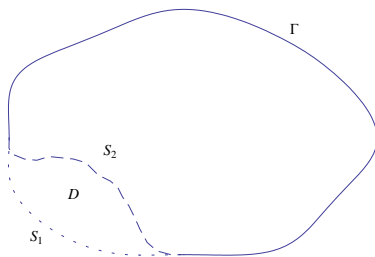


**Figure 3** An illustration of the region  $D$ , bounded by the surfaces  $S_1$  (dotted) and  $S_2$  (dashed).

We will assume sufficient smoothness of  $\partial D$  to permit integration by parts. Based on physical considerations, we will define the *optimal flux* as the flux  $g$  that maximizes the total heat entering the subdomain  $D$ . By virtue of (3)-(4) on  $\Omega_1$ , this amounts to maximizing the quantity  $|E(g)|$ , where

$$E(g) = \int_0^T \int_{S_2} \frac{\partial u_1}{\partial \eta} d\sigma dt = - \int_D u(T, x) dx, \quad (9)$$

where the last equality follows from (1)-(4) and Green’s identities.

For  $x \in \Omega_1$ , the solution  $u_1$  can be written as

$$u_1(t, x) = \int_0^T \int_{\Gamma} N_1(t - s, x, y) g(s, y) d\sigma_y ds,$$

where  $N_1(t, x, y)$  is the usual Neumann kernel for the heat equation, defined, for each fixed  $x \in \Omega_1$ , as the solution to

$$\frac{\partial N_1}{\partial t} - \Delta_y N_1 = 0, \quad x \in \Omega_1, \quad 0 < t < \infty;$$

$$\begin{aligned}\frac{\partial N_1}{\partial \eta_y} &= 0, \quad x \in \Gamma, \quad 0 < t < \infty; \\ N_1(0, x, y) &= \delta_x(y), \quad y \in \Omega_1.\end{aligned}$$

Substituting this representation into (9) yields

$$E(g) = - \int_0^T \int_{\Gamma} B_1(T-s, y) g(s, y) d\sigma_y dt, \quad (10)$$

where

$$B_1(t, y) \equiv \int_D N_1(t, x, y) dx.$$

From here, we explore two directions, which differ in the assumed properties of the input flux  $g$ .

### 3.1. “Heat Content” Approach: $L^2$ Formulation

Under the assumption that the input flux  $g$  belongs to the Hilbert space  $\mathcal{G}$  (with the same inner product (6)), it is clear from (10) that the maximum of  $|E(g)|$  occurs when  $g$  is a scalar multiple of  $B_1$ , i.e.

$$\hat{g}(s, y) = -c B_1(T-s, y), \quad \text{for some } c \in \mathbb{R}^+, \quad (11)$$

where the constant  $c$  is determined by the normalization requirement on  $g$ .

To construct this optimal flux  $\hat{g}$ , we simply solve an IBVP satisfied by  $B_1$ . Specifically,  $B_1(t, y)$  is easily shown to satisfy

$$\begin{aligned}\frac{\partial B_1}{\partial t} - \Delta_y B_1 &= 0, \quad y \in \Omega_1, \quad 0 < t < T; \\ \frac{\partial B_1}{\partial \eta_y} &= 0, \quad y \in \Gamma, \quad 0 < t < T; \\ B_1(0, y) &= \chi_D(y), \quad y \in \Omega_1,\end{aligned}$$

where

$$\chi_D(y) = \begin{cases} 1, & y \in D \\ 0, & y \notin D \end{cases}.$$

Figure 4 illustrates an example of this type of flux. In this example,  $\Omega_1$  and  $\Omega_2$  are the “capsule” domains described at the start of Section 4. The magnitude of the resulting optimal flux is plotted at several fixed times, as a function of  $x$ .

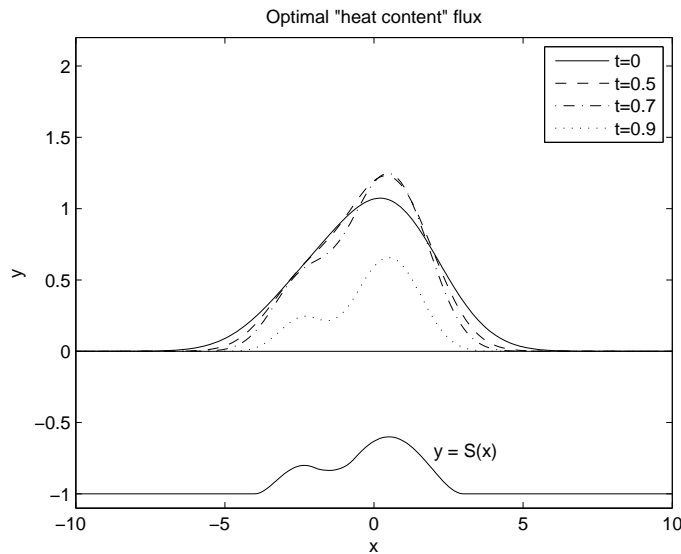


**Figure 4** An example of a flux constructed according to equation (11).

### 3.2. $L^2_*$ Formulation

In some thermal imaging applications, input heating is accomplished with low-intensity lasers. Thus motivated, we now consider input fluxes  $g$  of the form

$$g = g_0 + \sum_{j=1}^m c_j \delta_{t_j, x_j},$$

with  $g_0 \in L^2$ ,  $x_j \in \Gamma$ ,  $0 \leq t_j \leq T$ , and  $c_j \in \mathbb{R}$ . We normalize these fluxes according to

$$\sum_{j=1}^m |c_j| + \int_0^T \int_{\Gamma} |g_0| d\sigma_x dt = 1, \quad (12)$$

and denote by  $L^2_*$  the set of all such functions  $g$  for which the left-hand side of (12) is finite.

We have the following result:

**Theorem 3.1** *The normalized  $g \in L^2_*$  that maximizes  $E(g)$  is  $g = \hat{g}$ , where*

$$\hat{g}(t, y) = -\delta_{T-t_0, x_0}(t, y),$$

where  $(x_0, t_0)$  is a point on the closed and bounded region  $\bar{\Gamma} \times [0, T]$  where  $B(y, t)$  attains its maximum value  $M$ .

**Proof.** First, we show that  $E(\hat{g}) = M$ :

$$\begin{aligned} E(\hat{g}) &= - \int_0^T \int_{\Gamma} B_1(T-s, y) \hat{g}(s, y) d\sigma_y dt \\ &= \int_0^T \int_{\Gamma} B_1(T-s, y) \delta_{T-t_0, x_0}(s, y) d\sigma_y dt \\ &= B_1(T - (T - t_0), x_0) = B_1(t_0, x_0) = M. \end{aligned}$$



Next, we show that  $M$  is the maximum of  $E(g)$  on  $L_*^2$ , by showing that  $|E(g)| \leq M$  for all normalized  $g \in L_*^2$ . Indeed, for such a  $g$ , which may be written as

$$g = g_0 + \sum_{j=1}^m c_j \delta_{t_j, x_j},$$

with normalization (12), we have

$$\begin{aligned} |E(g)| &= \left| - \int_0^T \int_{\Gamma} B_1(T-s, y) \sum_{j=1}^m c_j \delta_{t_j, x_j}(s, y) d\sigma_y dt - \int_0^T \int_{\Gamma} B_1(T-s, y) g_0(s, y) d\sigma_y dt \right| \\ &\leq \left| - \sum_{j=1}^m c_j \int_0^T \int_{\Gamma} B_1(T-s, y) \delta_{t_j, x_j}(s, y) d\sigma_y dt \right| + \int_0^T \int_{\Gamma} |B_1(T-s, y) g_0(s, y)| d\sigma_y dt \\ &\leq \sum_{j=1}^m |c_j| |B_1(T-t_j, x_j)| + M \int_0^T \int_{\Gamma} |g_0| d\sigma_y dt \\ &\leq M \sum_{j=1}^m |c_j| + M \int_0^T \int_{\Gamma} |g_0| d\sigma_y dt \\ &= M \left( \sum_{j=1}^m |c_j| + \int_0^T \int_{\Gamma} |g_0| d\sigma_y dt \right) = M. \end{aligned}$$

So,  $|E(g)| \leq M$  for all normalized  $g \in L_*^2$ . Thus,  $\hat{g}(t, y) = -\delta_{T-t_0, x_0}(t, y)$  maximizes  $E(g)$ .  $\square$

#### 4. Numerical Examples

We now present the results of numerical experiments, designed to demonstrate the effectiveness of these “optimal” fluxes, within the context of the inverse problem introduced in Section 1. To describe the domain  $\Omega$ , we begin with the rectangular region defined in  $(x_1, x_2)$  coordinates by  $-10 \leq x_1 \leq 10$ ,  $0 < x_2 < 1$ , together with a half disk of radius  $1/2$  at each end, centered at  $(-10, 1/2)$  and  $(10, 1/2)$ . The domain  $\Omega$  consists of this region, but with the  $x_2 = 0$  (i.e. lower) portion of the surface replaced by the graph of  $x_2 = \sigma(x_1)$  for some function  $\sigma$  supported in the interval  $[-5, 5]$ . (See Figure 5.) The surface  $\Gamma$  consists of the top half (the connected portion of  $\partial\Omega$  lying above  $x_2 = 1/2$ ) of the boundary, and  $S_0$  the remainder.

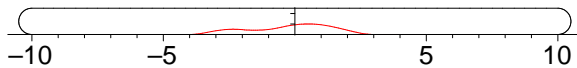


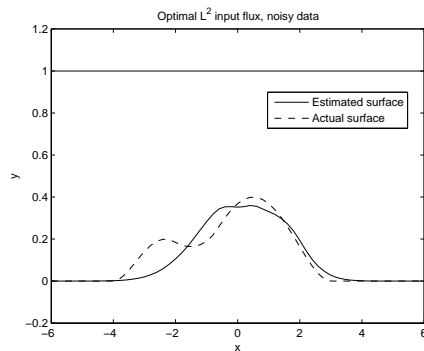
**Figure 5** The domain  $\Omega$  used in the numerical example.

To construct an optimal flux, we must specify a reference domain  $\Omega_1$ . Here, we will use a domain constructed analogously to  $\Omega$ , but with  $\sigma(x_1) \equiv 0$ . So, in the notation established in Section 2, we take  $\Omega_2 = \Omega$ , and use  $\Omega_1$  and  $\Omega_2$  to generate the input flux  $g(t, x)$ , to use for the inversion.

The forward problem is solved numerically, using boundary integral equations. We solve the inverse problem using the algorithm detailed in [2]. In each example, we use time interval  $(0, 1)$ , with the temperature  $u$  measured at points  $x_1 = -4 + 0.2k$ ,  $k = 0$  to  $k = 40$  on the top surface  $x_2 = 1$  (the interval  $[-4, 4]$  on the  $x_1$  axis) at each of times  $t = 0.05j$ ,  $j = 1$  to  $j = 20$ . At each data point (time/space) we add independent Gaussian random noise, standard deviation 0.2.

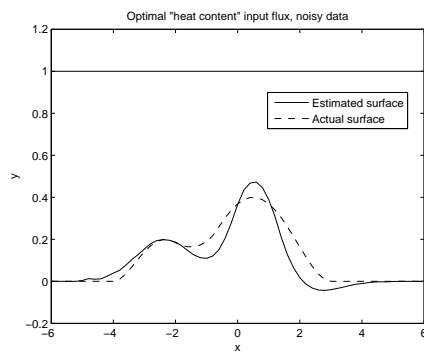
(For reference purposes, the temperature  $u$  typically lies in the range  $u = 1$  to  $u = 5$  over the course of the simulation.) The perturbation in the temperature, as compared to the uncorroded domain with back surface  $\sigma = 0$ , is about 0.5, so the noise is approximately 10 percent of the signal magnitude. In each figure in this Section, the dashed curve represents the true surface, and the solid curve represents the reconstruction.

Figure 6 shows the reconstruction that results from using the flux determined by Theorem 2.1.



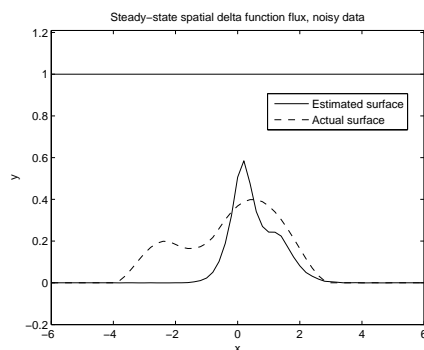
**Figure 6** *Reconstruction using the optimal input flux of Theorem 2.1.*

Figure 7 shows the reconstruction that results from using the flux defined by equation (11).



**Figure 7** *Reconstruction of back surface using the  $L^2$  “heat content” optimal flux of equation (11).*

Figure 8 is the same as the preceding two, but using the flux defined in Theorem 3.1.



**Figure 8** *Reconstruction of back surface using the flux from Theorem 3.1.*

For comparison, we show, in Figure 9, the corresponding results, when two other typical input fluxes are used. The first reconstruction was performed using a flux that is a delta-pulse

**Table 1.** Performance of input fluxes.

Flux	Figure	$\ u_1 - u_2\ _2$	$\ E(g)\ _2$	$\ S - S_0\ _2$
flux from Theorem 2.1	??	2.27	0.824	0.179
flux from equation (11)	??	1.32	1.0	0.190
flux from Theorem 3.1	??	—	—	0.334
$\delta$ at $t = 0$ , uniform in $x$	??a	0.67	—	0.260
uniform in $t$ and $x$	??b	0.32	0.541	0.387

at time 0, uniform in space. (This is representative of, e.g., flashlamp heating.) The second uses a flux that is uniform in both time and space.

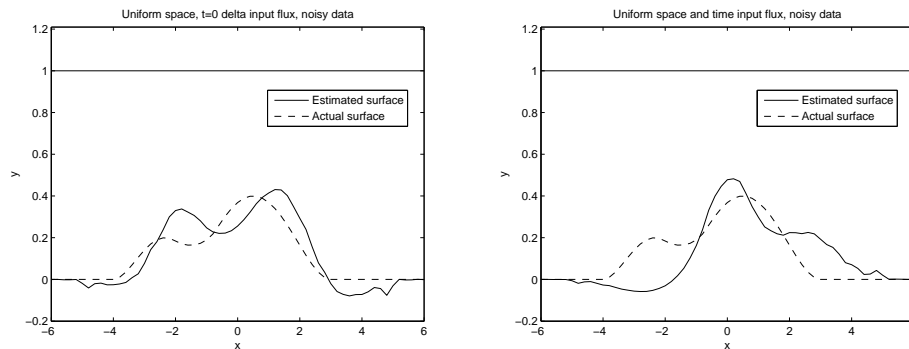


**Figure 9** Two examples, given for comparison purposes, of reconstructions resulting from other standard choices for input flux.

Table 1 provides further comparison of the performance of these various input fluxes. In this table, the column heading  $\|u_1 - u_2\|_2$  gives the  $L^2$ -difference in the measured data for the two surfaces. The column heading  $\|E(g)\|_2$  gives the total energy (as defined by equation (9)), scaled so that the largest value in that column is 1.0. The column heading  $\|S_1 - S_2\|_2$  measures the  $L^2$  error in the reconstruction of the surface  $S$ .

Some observations on these examples:

- The blanks in the table arise because the specific forms of some of these fluxes do not admit calculation of those quantities.
- As expected, the flux from Theorem 2.1 has the largest value of  $\|u_1 - u_2\|_2$ , since this is exactly the quantity that this flux was designed to maximize.
- For similar reasons, the flux from equation 11 has the largest value of  $\|E(g)\|_2$ .
- Of these five fluxes, the flux from Theorem 2.1 produces the smallest-error surface reconstruction.
- The performance of the flux from Theorem 3.1, despite the fact that it is designed to be optimal among those of its kind, is undeniably poor, providing only a rough indication of the location and magnitude of the most dominant difference between  $S_1$  and  $S_2$ . This suggests that a single laser pulse does not provide, even in the best case, sufficient information. One should instead consider a combination of such pulses, either sequentially or in unison.

## 5. Distinguishability

We return now to the setting of Section 2.1, and begin consideration the concept of *distinguishability by finite-precision measurements*, originally introduced in [8] for the impedance tomography problem. In the present context, our investigation begins with the following immediate corollary of Theorem 2.1.

**Corollary 5.1** *For every  $g \in B(\mathcal{G})$ ,*

$$\|L_1(g) - L_2(g)\| \leq \sqrt{\lambda_1}.$$

In words, this says that, for two given surfaces  $S_1$  and  $S_2$ , the difference in the measured data (i.e. the difference  $\|u_1(t, x) - u_2(t, x)\|$ ) is never larger than  $\sqrt{\lambda_1}$ , regardless of the choice of input flux. This, in turn, puts a limitation on the ability of practical data measurements to successfully distinguish between the two surfaces. Indeed, if the instrumentation used to measure the data on  $\Gamma \times [0, T]$  can measure only to precision-level  $\epsilon$ , and if  $\epsilon > \sqrt{\lambda_1}$ , then, up to measurement precision, *the measured data will be the same for both surfaces*, thereby rendering them indistinguishable from each other.

As an illustration, let  $\Omega_2$  be the rectangle  $[0, 1] \times [0, 0.5]$ , and let  $\Omega_1$  be the same rectangle, with a portion of its lower boundary replaced by a smooth symmetric hump, supported on the interval  $[0.4, 0.8]$ , and maximum height 0.2. For this pair of domains, we view the top boundary as  $\Gamma$  and the bottom boundaries as  $S_2$  and  $S_1$ , respectively. For this configuration, we compute that

$$\sqrt{\lambda_1} \approx 0.0539.$$

In light of the preceding corollary, this says that, if the data for each of these domains is measured with a device that is accurate only to the first decimal place, then, the measurements will be the same, and the differences between the two surfaces will not be detected.

Given the diffusive nature of heat, one may naturally ask how distinguishability, as measured by the eigenvalue  $\sqrt{\lambda_1}$ , changes with the height of the hump in the preceding example. One would expect that a shorter hump (or, more reasonably, a larger distance from the input boundary  $\Gamma$  to the back surface  $S_1$ ) would correspond to a smaller distinguishability. To investigate this, we consider the same domains as in the preceding example, and compare the distinguishabilities over a range of hump depths. As indicated in Figure 10, we denote the depth of the hump by  $d$ .

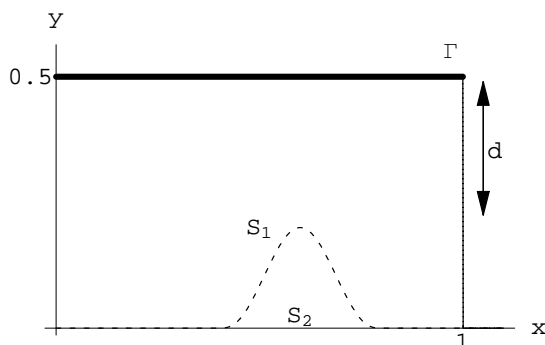


**Figure 10** *The geometry of the present situation.*

Figure 11 shows the value of  $\sqrt{\lambda_1}$  versus  $d$  for a range of  $d$ -values. For comparison, we also show the plot of the function  $\sqrt{\lambda_1} = 0.249e^{-5.025d}$ , the best-fit exponential function to this data. The fit is remarkably good, supporting the conjecture that, in this setting, the decay in distinguishability with respect to defect depth follows an exponential pattern, at least within the indicated range of  $d$ -values. (This is consistent with the results of similar experiments

previously performed for the electrical impedance tomography by a number of authors, e.g. [5].) The authors plan to pursue a systematic study of this relationship.

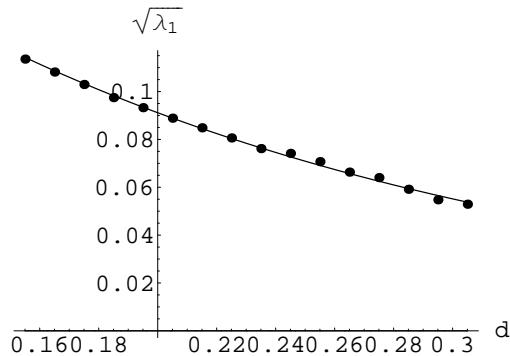


**Figure 11** Actual values of  $\sqrt{\lambda_1}$  vs.  $d$  (dots), and the plot of the best-fit exponential function (curve).

## 6. Concluding Remarks

Some final remarks are in order:

- In the field, one is limited, by available equipment (flashlamps, low-intensity lasers, etc.) in the specific thermal flux patterns that can be induced. Perhaps the flux patterns described in this paper would be best reproduced as discrete patterns, induced by a synchronized collection of laser pulses.
- Each of the three types of optimal fluxes introduced depends on the unknown boundary. In practice, one would desire an algorithm that will simultaneously recover both the flux and the boundary. This type of challenge has been addressed in other contexts (e.g. electrical impedance tomography), and tools developed there, such as the NOSER algorithm (see [?]), may serve as starting points for the present situation.
- As noted earlier, this is a report of preliminary findings, and there is much more work to be done. These encouraging results suggest that further research in this direction will be fruitful.
- We have set forth a number of methods for constructing useful input heat fluxes. In each method, it is necessary to specify the data time period (i.e. the time interval over which data will be collected) *before* constructing the input flux. The choice of this time window is another interesting design decision, and will be addressed in a future paper.

In the transition from theoretical mathematical results to practical implementation of those results, a number of design decisions must be made. In this paper, we have considered one such design decision, within a parabolic boundary determination problem. In addition to the practical necessity, consideration of such questions leads to interesting mathematics in its own right.

## Acknowledgments

This research was supported in part by the National Science Foundation under Grant #DMS-0104205.

## References

- [1] Bryan, K and Caudill, L 1998 Stability and reconstruction for an inverse problem for the heat equation *Inverse Problems* **14** 1429-53
- [2] Bryan, K and Caudill, L 2005 Reconstruction of an unknown boundary portion from Cauchy data in  $n$  dimensions *Inverse Problems* **21** 239-55

- [3] Cheney, M and Isaacson, D 1992 Distinguishability in impedance imaging *IEEE Trans. Biomed. Engr.* **39** 852-60
- [4] Cheney, M, Isaacson, D and Newell, J 1999 Electrical impedance tomography *SIAM Rev.* **41** 85-101
- [5] Cheney, M, Isaacson, D, Newell, J, Simske, S, and Goble, J 1990 NOSER: An algorithm for solving the inverse conductivity problem *Int. J. Imaging Syst. Technol.* **2** 66-75
- [6] Courant, R and Hilbert, D 1953 *Methods of Mathematical Physics, Vol. I* New York: Wiley
- [7] Dobson, D and Santosa, F 1994 Stability and resolution analysis of an inverse problem in electrical impedance tomography—dependence on input current patterns *SIAM J. Appl. Math.* **54** 1542-60
- [8] Isaacson, D 1986 Distinguishability of Conductivities by Electric Current Computed Tomography *IEEE Trans. Med. Imaging* **MI-5** 91-5
- [9] Isaacson, D and Cheney, M 1991 Effects of measurement precision and finite numbers of electrodes on linear impedance imaging algorithms *SIAM J. Appl. Math.* **51** 1705-31
- [10] Isaacson, E and Keller, H 1966 *Analysis of Numerical Methods* New York: Wiley
- [11] Ladyzenskaja, O, Solonnikov, V and Ural'ceva, N 1968 *Linear and Quasi-linear Equations of Parabolic Type* American Mathematical Society